

ASMCNN: An Efficient Brain Extraction Using Active Shape Model and Convolutional Neural Networks

Duy H. M. Nguyen^a, Duy M. Nguyen^b, Mai T. N. Truong^c, Thu Nguyen^d,
Khanh T. Tran^e, Nguyen A. Triet^f, Pham T. Bao^g, Binh T. Nguyen^{h,i,*}

^a*Max Planck Institute for Informatics, Germany*

^b*Dublin City University, Ireland*

^c*Department of Multimedia Engineering, Dongguk University, South Korea*

^d*Department of Mathematics, University of Louisiana at Lafayette, USA*

^e*Center for Machine Vision and Signal Analysis, University of Oulu, Finland*

^f*Department of Mathematics, University of Architecture of Ho Chi Minh City, Vietnam*

^g*Department of Computer Science, Saigon University, Ho Chi Minh City, Vietnam*

^h*Department of Computer Science, VNU-HCMUS, Ho Chi Minh City, Vietnam*

ⁱ*Vietnam National University, Ho Chi Minh City, Vietnam*

Abstract

Brain extraction (skull stripping) is a challenging problem in neuroimaging. It is due to the variability in conditions from data acquisition or abnormalities in images, making brain morphology and intensity characteristics changeable and complicated. In this paper, we propose an algorithm for skull stripping in Magnetic Resonance Imaging (MRI) scans, namely ASMCNN, by combining the Active Shape Model (ASM) and Convolutional Neural Network (CNN) for taking full of their advantages to achieve remarkable results. Instead of working with 3D structures, we process 2D image sequences in the sagittal plane. First, we divide images into different groups such that, in each group, shapes and structures of brain boundaries have similar appearances. Second, a modified version of ASM is used to detect brain boundaries by utilizing prior knowledge of each group. Finally, CNN and post-processing methods, including Conditional Random Field (CRF), Gaussian processes, and several special rules are applied to refine the segmentation contours. Experimental results show that our proposed method outperforms current state-of-the-art algorithms by a significant

*Corresponding author

Email address: ngtbinh@hcmus.edu.vn (Binh T. Nguyen)

margin in all experiments.

Keywords: skull stripping, brain extraction, Convolutional Neural Network, Active Shape Model, Conditional Random Field, Gaussian processes

1. Introduction

Whole brain segmentation is the problem of extracting brain regions from volumetric data, such as Magnetic Resonance Imaging (MRI) or Computed Tomography (CT) scans. It resulted in segmentation maps indicating parts of brain after removing non-brain tissues such as eyes, fat, bone, marrow, and dura. Brain extraction is the prior step in most neuroimaging analysis systems, which usually consists of brain tissue classification and volumetric measurement [1], template construction [2], and cortical and sub-cortical surface analysis [3]. Early preprocessing steps such as the bias field correction can also benefit from brain extraction [4]. Therefore, brain extraction needs to be considered before producing high-performance methods.

Automatic skull stripping reduces processing time and prevents any human bias in the final results, especially in large-scale studies, where thousands of images with different characteristics and significant anatomical variations need to be examined. Most skull-stripping methods are optimized and validated for MRI T1-weighted images since high-resolution T1-weighted structural images are prevalent in clinical studies [5], and they provide excellent contrast between different brain tissues. Existing brain extraction methods can be categorized as edge-based, template-based, label fusion with atlas-based, non-local patch-based [6], and recently, deep learning-based approaches.

Edge-based methods focus on detecting edges between the brain region and the non-brain region by considering differences in these structures' appearance. Several techniques have been employed, such as watershed [7], level set [8], histogram analysis [9], etc. Although these methods have proven their effectiveness and achieved comparable results, their performance tends to be less accurate when working with pathology, different sites, scanners, and imaging acquisition

protocols [10].

Template-based methods register a subject to a template via affine transformation [11] or deformable models [12] to create an initial estimation for the brain mask. After that, the boundary of the brain mask is segmented again by
30 one classifier to increase the accuracy of the final results. Templates can involve one or more distinctive atlases. Therefore they are robust, stable in different conditions, and highly accurate.

Label fusion with atlas-based techniques, such as Multi-Atlas Propagation
35 and Segmentation (MAPS) [13], Advanced Normalization Tools (ANTs) [14], and Pincram [15], implement registration of multiple atlases to a target subject by using deformable models. After being registered to the target space, one can combine brain masks in all atlases using Simultaneous Truth And Performance Level Estimation (STAPLE) [16] or joint label fusion. Since these approaches’
40 primary operations are registration processes, their performance depends on the accuracy of the registration ones and the quality of the brain mask in each atlas. Also, the variability representation in brain anatomy usually requires a large number of atlases. Hence these methods are typically time-consuming and computationally intensive.

45 Non-local patch-based methods first transform atlases to subject spaces using appropriate affine registrations to estimate the subject’s initial brain mask. A neighborhood searching process for each small patch, which is around the initial estimation of the brain boundary, is performed. Finally, patches are associated together, and similarity weights can be computed to generate the final
50 brain mask. Several methods, such as Brain Extraction using non-local Segmentation Technique (BEAST) [17], Multi-cONtrast brain STRipping (MONSTR) [6] are inspired by this idea, and they achieve remarkable performance in aspects of both accuracy and robustness. However, one difficulty of this approach is pinpointing the optimal setting for parameters, including the number of atlases or
55 the window size. Additionally, in T1-weighted atlases, the intensity values of structures such as hemorrhages, tumors, or lesions may be similar to that of non-brain tissues. Non-local based methods use different MRI acquisition pro-

protocols to obtain complementary information and overcome this challenge. As a result, it is a complex task and requires more processing time.

60 Recently, deep learning has become a hot trend in many fields, including neuroimaging. Unlike traditional methods, deep learning is more reliable, robust, and able to produce superior performance in pattern recognition. One of the most popular systems using a deep-learning approach in neuroimaging is U-Net [18]. In this method, one contracting path and another symmetric
 65 expanding path are used for capturing context and precise localization, respectively. U-Net can use available annotated samples more efficiently by utilizing data augmentation for the training phase. Kleesiek and colleagues [19] propose a 3D convolutional deep learning architecture for skull stripping. This method can deal with pathologically altered tissues and different modalities; hence it
 70 can be applied to several types of MRI data. Hao Dong and collaborators [20] present a fully automatic scheme that can detect and segment brain tumors simultaneously using the U-Net based deep convolution networks. The experiments on the BRATS 2015 challenging [21] demonstrated that their method could provide both efficient and robust segmentation compared to the manual
 75 delineated ground truth. Other studies can be found at [22, 23].

In this research, we present a novel approach for brain extraction in T1-weighted MRI data by combining ASM [24] and CNN [25], namely ASMCNN. Unlike existing methods, we consider the brain extraction problem as a segmentation task for 2D image sequences in the sagittal plane rather than working
 80 with 3D structures. Our approach has several benefits. First, it allows us to develop specific algorithms for different brain boundary silhouettes. Throughout image sequences, shapes of brain boundaries and brain sizes vary significantly, especially for sagittal slices located at the beginning and ending parts of 3D MRI volumes, where brain regions are small, and the corresponding boundaries
 85 are very complex. Based on prior knowledge about brain structures [26], we develop specific rules to control the segmentation process effectively. Second, images in the sagittal plane are symmetrical across two hemispheres. By utilizing this property, we can predict the brain mask’s general shape based on

slices’ positions. This property also enables us to establish more extensive and
90 accurate rules for segmentation.

The main contributions of our work can be summarized as follows:

1. Our approach is motivated by the divide-and-conquer idea; thereby, we
group 2D-images into different groups by exploiting the brain’s symmetry
in the sagittal plane. Each group is then designed to obtain optimal
95 predictions that satisfy both global, local information, and prior medical
knowledge.
2. CNN, with high-level feature representations, is utilized to refine brain
boundaries. Besides, global spatial information of each voxel is combined
with features computed from convolutional neural networks. Hence, our
100 method can represent both global and local features simultaneously.
3. We make use of the similarity of brain contours in each group by applying
ASM to detect general properties of boundaries. This procedure guaran-
tees each object’s geometrical attributes and enhances the overall accuracy
of segmentation results.
- 105 4. Our framework does not depend on any specific MRI format, and there-
fore, it can be applied effectively in different acquisition conditions.

The remainings of this paper are organized as follows. In Section 2, we
introduce all necessary notations and present an appropriate architecture and
algorithms for the problem. After that, we compare our approach with seven
110 state-of-the-art methods on three public datasets in Section 3. The Section 4
is devoted to discuss strengths and major limitations of ASMCNN as well as
future research directions. Finally, we end the paper by a brief conclusion.

2. Methodology

In neuroimaging, one can use a three-plane coordinate system to describe
115 a human body’s standard anatomical position. These imaging planes are the
transverse plane, the sagittal plane, and the coronal plane. In ASMCNN, we
choose to process 2D slices in the sagittal plane as human brains are nearly

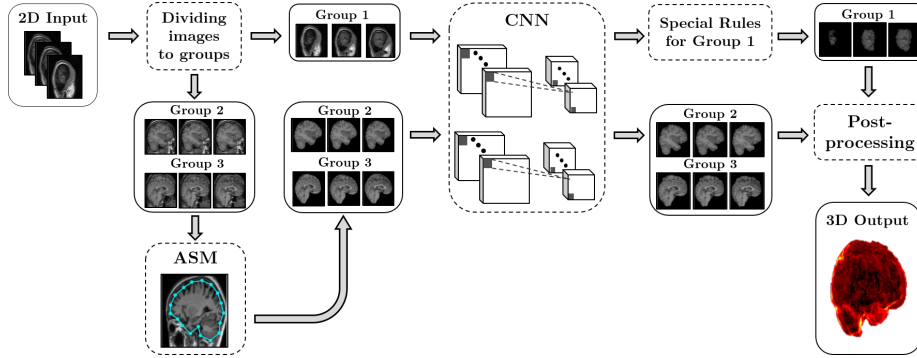


Figure 1: An overview of our proposed method with 2D input and stacking predicted results to obtain a 3D volume. Firstly, images with similar shape and appearance are divided into three distinct groups, namely Group 1, Group 2, and Group 3. Secondly, to obtain initial masks for all groups, a modified Active Shape Model (ASM) is then applied for Group 2 and Group 3, while a Convolutional Neural Network (CNN) is utilized in Group 1 due to its complex shape with disconnected regions. Thirdly, over-smooth results in Group 2 and 3 are corrected by the CNN (same architecture used in Group 1) for pixels locating near the object’s boundary. With Group 1, prior medical knowledge from brain positions and obtained masks in Group 2, 3 are integrated by special rules to eliminate noisy regions, e.g., skull areas. Finally, all results are post-processed by a conditional random field to alleviate fatal errors by pixel-wise approaches.

symmetrical concerning the mid-sagittal plane. It allows us to predict the general shapes of brain regions with better accuracy. ASMCNN comprises of three
 120 main stages: (1) dividing images into groups, (2) applying ASM to detect initial brain boundaries for images in specific groups, and (3) constructing CNN for precise segmentation, along with performing different post-processing methods for different groups to refine segmentation contours. The flowchart of our system is given in Figures 1. Three main stages of the proposed method are presented
 125 in the following subsections.

2.1. Sagittal-slice classification

In the first stage, we divide sagittal slices into several groups by initial analysis of brain regions’ shapes. We categorize slices into three groups based on their general shape, entitled Group I, II, and III. In Figure 2, we illustrate a
 130 few slices in each groups. It is clear that the brain region in Group I is quite

small compared to the image size. Meanwhile, the brain areas in Group II and Group III are relatively large, and the brain regions in Group III extend out at the lower-left corner of images. For taking advantage of the symmetry of the human brain across the sagittal plane, we assign the corresponding group of each slice by the following order: Group I, Group II, Group III, Group II, and Group I. Figure 3 depicts how three groups distribute throughout the sagittal axis.

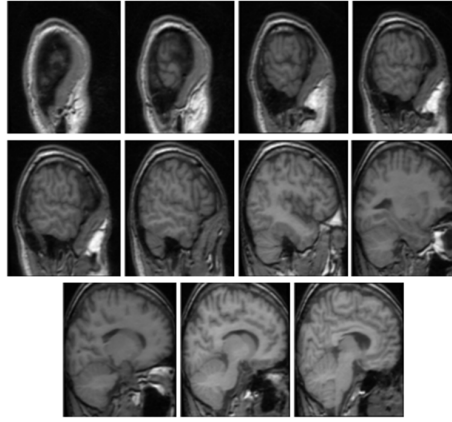


Figure 2: Typical appearances of each group. Top row: group I; middle row: group II; bottom row: group III.

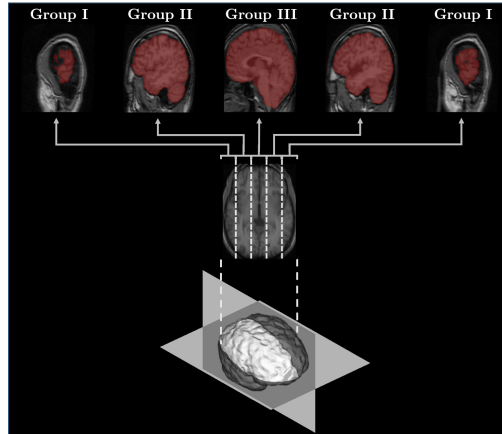


Figure 3: The illustration of the order of three groups in the sagittal plane.

We construct a grouping method by using histograms of oriented gradients

(HOG) [27] extracted from a sub-rectangle to train a soft-margin Support Vector
Machine (SVM) classifier [28] (Algorithm 1). The sub-rectangle in Algorithm 1
140 is illustrated as yellow rectangles in Figure 4, which are 30% area at the bottom
of the red bounding boxes, indicating the signature differences between brain
shapes. Figures 4a and 4b are two adjacent slices from Group II and Group
I, respectively. As shown in these figures, the brain in Figure 4a has a small
145 tail at the lower left part, while the brain in Figure 4b does not. This example
shows that brain shapes can be significantly different even though the slices are
adjacent. Similarly, Figures 4c and 4d are two adjacent slices from Group II
and Group III. Here, the brain shape in Group II is more convex, while the one
in Group III is concave at the lower right part. We utilize these differences to
150 construct a robust classification method using SVM. Algorithm 2 can be used
to classify sagittal slices of MRI volumes into different groups by using the SVM
model trained by Algorithm 1. The notations of Algorithms 1 and 2 are depicted
in Table 10.

After grouping images, we perform various procedures for each group. For
155 Group I, as the brain shape is complex and the brain regions are smaller than
those in other groups, it is challenging to propose a general model for brain
shapes. Therefore, we use CNN to process all pixels in the images, directly
predict the brain regions. We utilize special rules and the Gaussian process to
refine the results from the CNN further after predicting with CNN. For Group
160 II and III, we first apply ASM to produce the initial brain boundaries. Then
pixels locating around the boundaries are fed to a CNN for precise segmentation.
Finally, we perform post-processing using CRF for all groups, producing high-
quality segmentation results. In the next section, we present the details of ASM
for estimating initial brain contours for Group II and Group III.

165 2.2. Active shape model with optimal features

We apply ASM to slices in Group II and III, producing rough segmentation
of brain regions in this stage. For enhancing the modeling capacity of gray-level
variations around the border, we use a modified version of ASM called Active

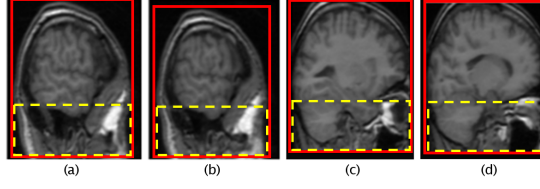


Figure 4: Sub-rectangles and differences between brain shapes in different groups.

Shape Model with optimal features (ASM-OF) [24]. It is worth noting that optimal displacements for landmarks in the original ASM algorithm can be replaced by using a nonlinear k-nearest neighbor classifier (k-NN, [29]) instead of using the linear Mahalanobis distance [30]. We denote all necessary annotations used in the ASM-OF algorithm in Table 1. This stage comprises three subroutines, and we illustrate each subroutine in the following paragraphs.

Table 1: List of notations used in Active Shape Model with optimal features.

Notation	Remark
s	the number of training images.
n	the number of landmark points used to represent each image.
n_s	the number of new positions evaluated during searching.
k	the number of points in profile located either inside and outside of the landmark point.
l_{max}	the number of resolution levels for appearance model.
n_{grid}	the size of $n_{grid} \times n_{grid}$ of points, which are sampled in training process.
n_{max}	the number of iterations per resolution level.
k_{NN}	the number of neighbors used in k-NN classifier during searching and feature selection.
f_v	a chosen proportion of the shape variance in the training dataset.

2.2.1. Our proposed shape model

Normally, a brain image with s sagittal images can be represented by a set of vectors X_i by stacking n landmarks $((x_1, y_1), \dots, (x_n, y_n))$ as:

$$X_i = (x_1^i, y_1^i, \dots, x_n^i, y_n^i)^T \text{ where } i \in [1, s]. \quad (1)$$

One can use the principal component analysis (PCA) method to calculate the mean shape \bar{X}_s , the corresponding covariance matrix C , the first t largest eigenvalues λ_m and eigenvectors ϕ_m ($m = 1, \dots, t$) of C . After that, a brain shape in the training data set can be approximated by:

$$X_s \approx \bar{X}_s + \Phi_s \mathbf{b}_s, \quad (2)$$

where $\Phi_s = (\phi_1 \dots \phi_t)$ is the first t eigenvectors and $\mathbf{b}_s = \Phi_s^T (X_i - \bar{X}_s)$ is a set of shape parameters, \mathbf{b}_s can be bounded by

$$-q\sqrt{\lambda_i} \leq \mathbf{b}_s \leq q\sqrt{\lambda_i} \quad (i = 1, \dots, t), \quad (3)$$

where $q \in [2, 3]$ [30]. The value of the parameter t can be chosen so as to explain a certain proportion f_v of the variance in the training shapes, which usually has a range from 90% to 99.5%. For a given f_v , one can experimentally choose the smallest non-negative integer t such that

$$\sum_{i=1}^t \lambda_i \geq f_v \sum_{i=1}^{2n} \lambda_i. \quad (4)$$

2.2.2. A gray-level appearance model with optimal features

We use a gray-level appearance model to describe a typical image structure around each landmark by applying a k-NN classifier from pixel profiles. These
180 are sampled by using the linear interpolation method around each landmark, which is perpendicular to the contour. From each training image, for each landmark, we define a square grid of $n_{grid} \times n_{grid}$ points in which n_{grid} is chosen as an odd integer, and the landmark point is at the center of the grid. In experiments, n_{grid} is selected as 5; hence, a feature vector has 60 elements,
185 which are calculated at 25 points. The output of each feature vector is a binary

value, which is 1 in the case it is inside the object or 0 for other cases. The k-NN classifier with the corresponding weight to each vote is $\exp(-d^2)$, where d is the Euclidean distance to each neighbor in the feature space. Mann-Whitney algorithm [31] is used to select the best feature.

Given an input image, each position along the profile is calculated, yielding 60 feature images and processed again to create optimal features. These features are then fed into the k-NN classifier to determine the probability of being inside the object for this pixel. Then, we determine the point g_i in the set of points of the profile g such that the objective function $f(g)$ is minimized as

$$f(g) = \sum_{i=-k}^{-1} g_i + \sum_{i=0}^{+k} (1 - g_i) \quad (5)$$

190 where $g_i \in [-k, k]$ is oriented from the outside to the inside of the object.

2.2.3. Model evolution

After the shape model and the k-NN classifier are constructed from the training dataset, the ASM-OF can be applied to segment objects as follows.

- Step 1. Initialize the shape model with \bar{X}_s .
- 195 • Step 2. For each landmark, put it at $2n_s + 1$ new locations and evaluate the equation (5) with the k-NN classifier to find and move it to a new position denoted is X_{New} .
- Step 3. Fit the shape model by calculating \mathbf{b}_{sNew} using (2.2.1) as (6), and limit values of \mathbf{b}_{sNew} using (3):

$$b_{sNew} = \Phi_s^T (X_{New} - \bar{X}_s) \quad (6)$$

200 where $X_{New} = (X_{1New}, X_{2New}, \dots, X_{nNew})$.

- Step 4. Update the shape landmarks using (2) as

$$X_{sNew} \approx \bar{X}_s + \Phi_s \mathbf{b}_{sNew}$$

- Step 5. Iterate steps 2 and 4 up to a predefined n_{max} times.

Since ASM-OF can only capture general shapes of the brain region, derived boundaries are very smooth. Therefore, in the next stage, we utilize a CNN for exact segmentation of results from ASM-OF to accurately localize the boundary of the brain region.

2.3. Convolutional neural networks

In this section, we present the structures of the CNNs. For Group I, one CNN focuses on all pixels in the brain image and directly identifies pixels belonging to the brain regions. For Group II and III, we construct another CNN which focuses on pixels located around the boundary of the preliminary brain mask estimated from the previous stage instead of using all pixels. Additionally, we also exploit the global spatial information [32] and combine it with the feature maps learned from CNN as an input vector for multi-layer perceptrons. We describe the architecture of the proposed CNN in the following sections.

2.3.1. Input and output space

Assume that N is the number of slices of an MRI volume, $I_1 = \{I_{11}, \dots, I_{1p}\}$, $I_2 = \{I_{21}, \dots, I_{2q}\}$, $I_3 = \{I_{31}, \dots, I_{3r}\}$ are the sets of images in Group I, II, and III respectively, where $p + q + r = N$, $M_2 = \{M_{21}, \dots, M_{2q}\}$, $M_3 = \{M_{31}, \dots, M_{3r}\}$ are the sets of brain masks produced by ASM for Group II and III. For each image in Group II and III, positions of pixels around the boundary of M_i ($i \in \{2, 3\}$) with the distance around 5 pixels are extracted by using the algorithm 5 (Figure 5). These positions are then extracted the information based on I_j ($j \in \{2, 3\}$). With images in I_1 , all pixels within the rectangle, which contains the skull, are used as features. We aim to employ CNNs to predict each pixel belonging to a brain or non-brain region.

To this end, we extract two following features representing each pixel. First, we consider local features, which are three adjacent image slices of the size 11×11 centered around each pixel. Next, we calculate global features by combining the position (x, y) of each pixel and the index z of the corresponding image

where pixel belongs to $(1 \leq z \leq N)$. Figure 6 illustrates detailedly the feature extraction process and how to combine two features in the network.

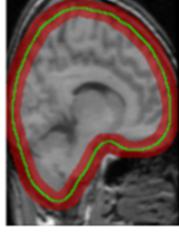


Figure 5: Preliminary brain boundary produced by ASM (green) and surrounding pixels that are classified by CNN (red).

2.3.2. A proposed CNN architecture

Figure 6 describes our network structure. It includes three convolutional
 235 layers followed by four fully connected layers, including the final two-node layers
 for the output. The size of the convolutional layers is 3×3 , and the max-pooling
 layers use 2×2 kernel. We choose the depths of the first, the second, and the
 third convolutional layers as 13, 26, and 39, respectively. The ReLU activation
 function ($f(x) = \max(0, x)$) is applied to outputs of the convolutional layer.

240 After that, three vectors from three slices of images obtained from convo-
 lutional layers can be concatenated with the normalized coordinates to form a
 new vector. This vector is later fed into the fully connected layers. The depths
 of four fully connected layers are 574, 300, 50, and 2, consecutively. The final
 layer has the size of two, indicating the probability of the input pixel belonging
 245 to the brain or non-brain region.

2.3.3. Training and Optimization

The aim of CNN is to minimize the L_2 penalized cost function:

$$L(w) = \frac{1}{n} \sum_{i=1}^n l(z, f(x, w)) + \frac{\eta}{2} \|w\|^2, \quad (7)$$

for a labeled training set (x_i, z_i) , $i \in (1, n)$ and weights (w_1, \dots, w_L) including
 convolutional kernel weights and bias weights with a loss function l . The loss

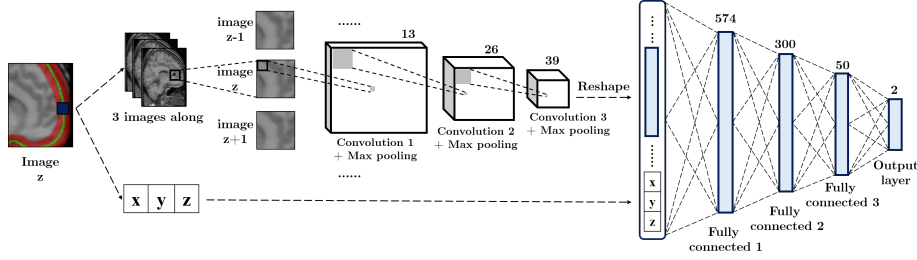


Figure 6: Feature extraction step and the proposed deep neural network structure.

function l can be defined as:

$$l(z, f(x, w)) = -\frac{1}{N_1} \sum_{n=1}^{N_1} \sum_{m=1}^{M_1} B_{m,n} \log(p_{m,n}) \quad (8)$$

where N_1 is the number of training images in the batch, M_1 is the number of classes, and $p_{m,n}$ is the probability of the n -th sample being classified into the m -th class. If the n -th sample is classified into the m -th class, $B_{m,n}$ equals to 1, otherwise $B_{m,n}$ is 0. We fix $\eta = 0.005$ and learn the weights by using Adam optimizer. All weights in each layer at the convolutional layer are initialized from a normal distribution of $N(0, 0.1)$ while weights in multi-layer perceptrons are created from a normal distribution of $N(0, \frac{1}{n_{hidden}})$ where n_{hidden} is the number of hidden layers of the previous layer [33]. The CNN is trained by using mini-batch stochastic gradient descent with a batch size of 128. For preventing over-fitting, we use a dropout layer after each layer in the fully connected layers with the rate 50%.

2.4. Special Rules for Group I

Brain regions in Group I are small and noisy, which might be cases that CNNs produce two regions in the segmented results, as demonstrated in Figure 9. However, it is difficult to determine which area is the brain region automatically. To overcome this, we utilize Gaussian processes [34]. Gaussian processes are used to learn the change in positions of the brain center points throughout sagittal slices. Based on this change, we can predict the center of cerebral images in Group I. Then, the area closest to the center of the gravity is selected for execution.

Figure 7 illustrates training results with the IBSR dataset [35] by Gaussian processes. The blue lines illustrate the change of the center position of cerebral ventricles for each subject from the starting position to the ending position; here, 12 blue lines indicate 12 subjects. It is worth noting that the positions of the starting slice and the ending slice in MRI volumes are not consistent. Therefore, we normalize the starting and ending slice indexes to $[1, 100]$ as visualized on the x-axis (Figure 8). The y-axis represents the norm-2 of the center position of the brain images from the training data. The red line illustrates the result of Gaussian processes at 50 different normalized slice indexes.

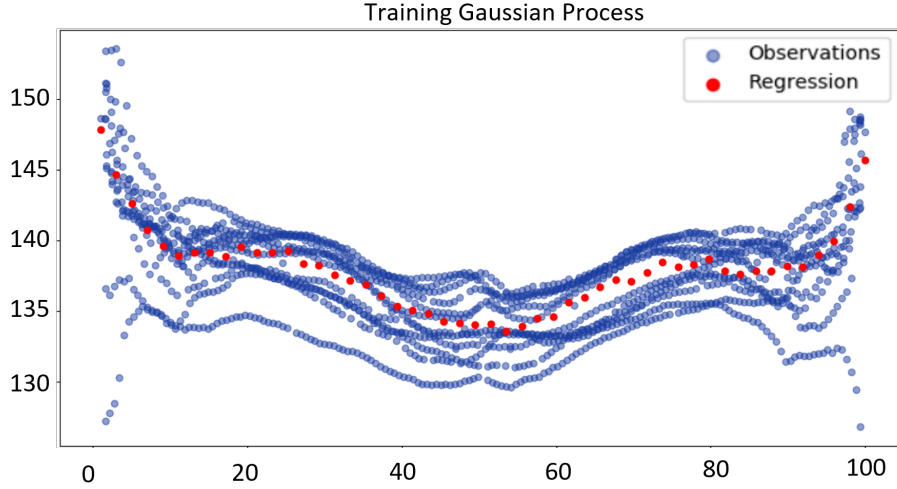


Figure 7: Illustration for training process of Gaussian processes in the IBSR dataset.

Figure 8 depicts the predicted results by Gaussian processes. The red line illustrates the Gaussian processes' initial prediction for a new subject. After adjusting this prediction, we obtain the blue line, which is the final result of the Gaussian processes. The purple line is the ground truth. The adjustment for predictions from the Gaussian processes is based on two factors:

- By various image acquisition conditions, an image of a subject can be shifted but usually, the changing rate of the image center along each slice may remain unchanged. Hence, it is possible to correctly predict the center

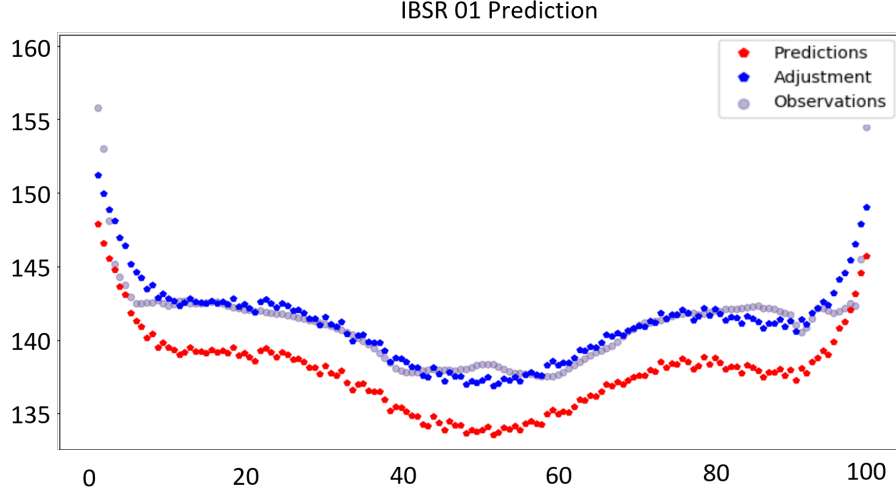


Figure 8: Predicted results of Gaussian processes in the IBSR dataset.

of the brain region by translating the initial prediction with a value α .

- For each subject, one can firstly combine ASM-OF, CNN, and CRF to detect two regions II and III. Next, one can consider centers of all images in both two regions, compare the deviation among predicted results by Gaussian processes, and compute the mean value as a desired value of α .

After doing the translation and obtaining the blue line, for each slice in Group I, we calculate the distance between each connected component and the predicted value of Gaussian processes and select the region with the shortest distance. The algorithm 4 describes detailedly how images in Group I are processed. The list of its sub-algorithms including *CheckCenter* (6), *CheckArea* (7), *ConvertRange* (3), and *CheckDistance* (8) are presented in Appendices and *CRF* is presented in the section 2.5.

2.5. Post-processing

In this stage, we apply post-processing techniques for further refining segmented slices from all groups. Because all main procedures are pixel-wise approaches, segmentation maps are not smooth and precise, which can decrease

300 the overall accuracy of the brain extraction process significantly. To overcome this issue, we utilize a post-processing technique based on the conditional random field (CRF) to validate the extracted results from both ASM-OF and CNN and to refine these segmentation maps.

Let \mathbf{I} be an image of size $N_2 \times N_2$ and \mathbf{x} be its segmentation map. The Gibbs energy of \mathbf{x} can be given by

$$E(\mathbf{x}) = \sum_i \varphi_u(x_i) + \sum_{i < j} \varphi_p(x_i, x_j) \quad (9)$$

where x_i and x_j are labels assigned to the i -th and j -th pixels, respectively. Here, the label is 1 when the pixel in the “brain” region and 0 for other cases. The unary potential is given by $\varphi_u(x_i) = -\log P(x_i)$, where $P(x_i)$ is the probability of pixel i getting classified as “brain”, and is estimated from the output of the main procedure. Denoting p_i, I_i are the position and the grey value features of pixel i , we use the contrast-sensitive two-kernel pairwise potential $\varphi_p(x_i, x_j)$ as in [36],

$$\psi_p(x_i, x_j) = \mu(x_i, x_j) \left[\exp \left(-\frac{|p_i - p_j|^2}{2\theta_\alpha^2} - \frac{|I_i - I_j|^2}{2\theta_\beta^2} \right) + \exp \left(-\frac{|p_i - p_j|^2}{2\theta_\gamma^2} \right) \right], \quad (10)$$

where $\mu(x_i, x_j) = [x_i \neq x_j]$ is the Potts model compatibility function that 305 captures the compatibility between different pairs of labels, parameters θ_α , θ_γ and θ_β control the degrees of the nearness and appearance similarity. In our experiments, we set $\theta_\alpha = (8, 11)$, $\theta_\beta = (8, 8)$.

The most probable segmentation map \mathbf{x}^* is calculated by

$$\mathbf{x}^* = \arg \min_{\mathbf{x} \in \mathcal{L}^N} E(\mathbf{x}) \quad (11)$$

where $E(x)$ is minimized by the mean-field approximation as described in [36]. The visualization of all stages from CNN to post-processing steps for Group I 310 and Group II, III are illustrated in Figures 9 and 10 respectively.

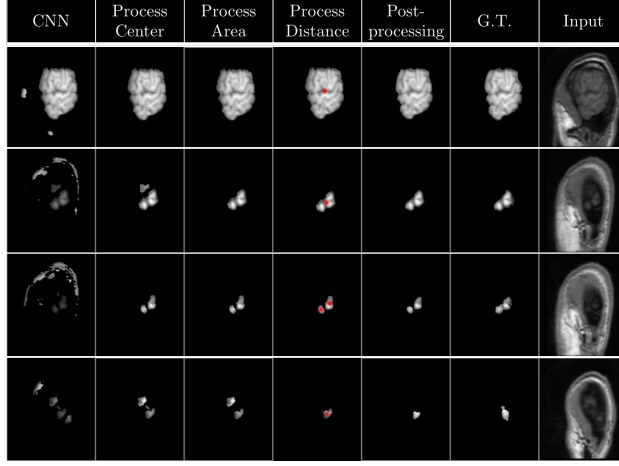


Figure 9: Processing steps for Group I.

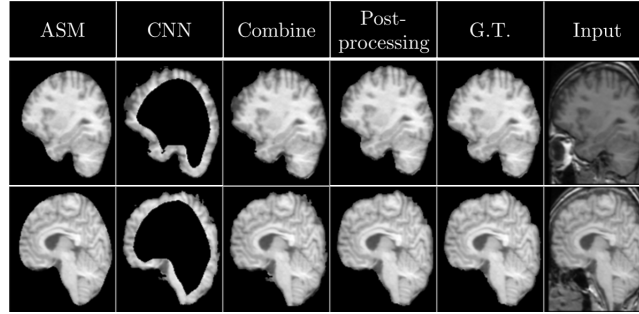


Figure 10: Processing steps for Group II and Group III.

3. Experiments

3.1. *ASMCNN versus others*

We compare our proposed approach with seven well-known methods, including Brain Extraction Tool (BET) [37], Brain Surface Extractor (BSE) [38], 3DSkullStrip (3DSS) [39], ROBEX [11], Brain Extraction based on nonlocal Segmentation Technique (BEAST) [17], 3D-CNN [19], and U-Net approach [20]. All necessary implementations are optimized to work with T1-weighted data. Based on codes released by Hao Dong et al. [20], we adopt the proposed network to train end to end with 2D image sequences in the sagittal plane, denoted as 2D-Unet. For 3D-CNN by Kleesiek et al., we only extract the final results

mentioned in [19] for the comparison in the chosen datasets. We evaluate the performance of all these methods by three publicly available datasets: Internet Brain Segmentation Repository (IBSR) [35], LONI Probabilistic Brain Atlas (LPBA) [40], and the Open Access Series of Imaging Studies (OASIS) project [41]. We use 6 out of 20 subjects in the IBSR dataset for training and validation in this work, and all 14 remaining subjects are chosen for testing. Similarly, 12/28 is the ratio between the number of training and testing subjects in the LPBA dataset, and 22/55 is the corresponding ratio for the OASIS dataset.

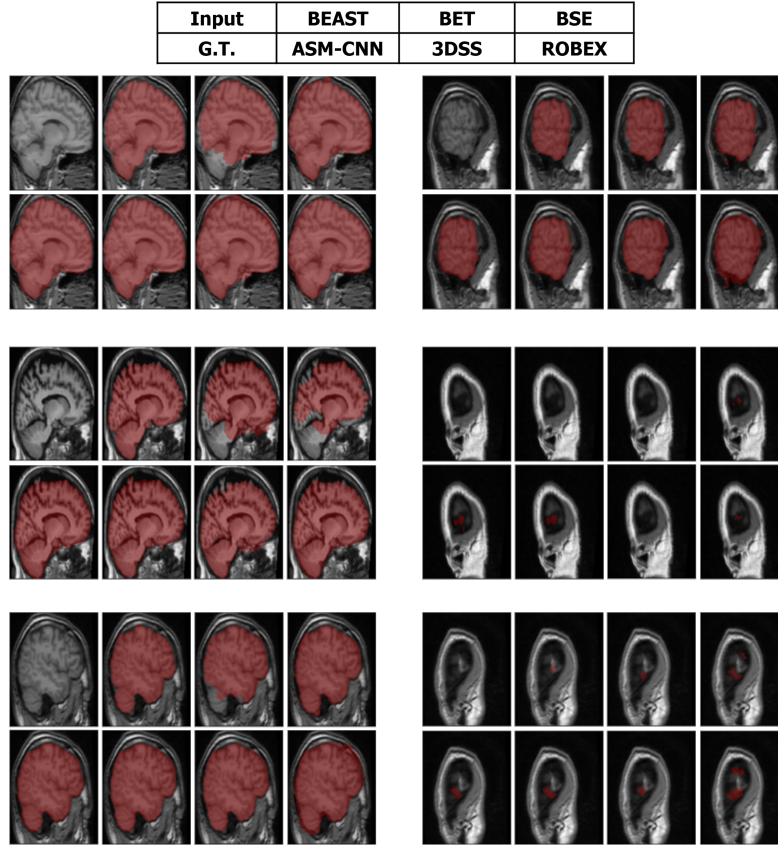


Figure 11: The comparison between ASMCNN with other methods on IBSR dataset.

3.2. Settings and metrics

330 We implement the proposed system in Python with the TensorFlow library [42] for feature extraction and training deep neural networks. The architecture of deep neural networks is described in Figure 6, with the ReLU activation function for all three datasets. To avoid over-fitting, we add dropout layers with a rate of 50% after each layer in a deep neural network. The training 335 phase took approximately 0.8 hours for IBSR, 1.6 hours for LPBA, and 3.2 hours for OASIS to complete. This process has been performed on a workstation equipped with Intel(R) Xeon(R) E5-2698v4 CPU running at 2.20Ghz and an NVIDIA GeForce GTX 1080 GPU. The average time for processing one single MRI volume in the testing phase is approximately 48 seconds. We evaluate 340 all brain extraction methods' performance by comparing segmentation results with the ground truth in each dataset using the Dice coefficient, Jaccard index, Average Hausdorff Distance (AHD), Sensitivity score, and Specificity score [43].

3.3. Qualitative evaluation

Segmentation results of ASMCNN and seven other methods in the sagittal 345 plane for the three datasets are illustrated in Figures 11, 12 and 13 respectively. Each figure includes six typical testing scans from all three groups (two scans for each group). Although ASMCNN works with the sagittal plane, it also produces correct segmentation in two other planes. Figure 14 shows the comparison between our approach and other methods on each dataset for these two planes.

350 ASMCNN can provide extremely accurate segmentation in these three datasets. We achieve the same results as ROBEX with smooth boundaries and keep both gray and dura matter inside extracted brains for most cases, which are usually left out by ROBEX. Although there are minor leakages into the skull by ASMCNN, its occurrence is less than both ROBEX and BEAST, as it only 355 generates a smaller number of over-segmentation results. The critical impact of the method is that it can precisely work for small-size brains in Group I as well, meanwhile other techniques usually fail. As shown in Figures 11 - 13, our results are mostly similar to the ground-truth images especially for tiny-size

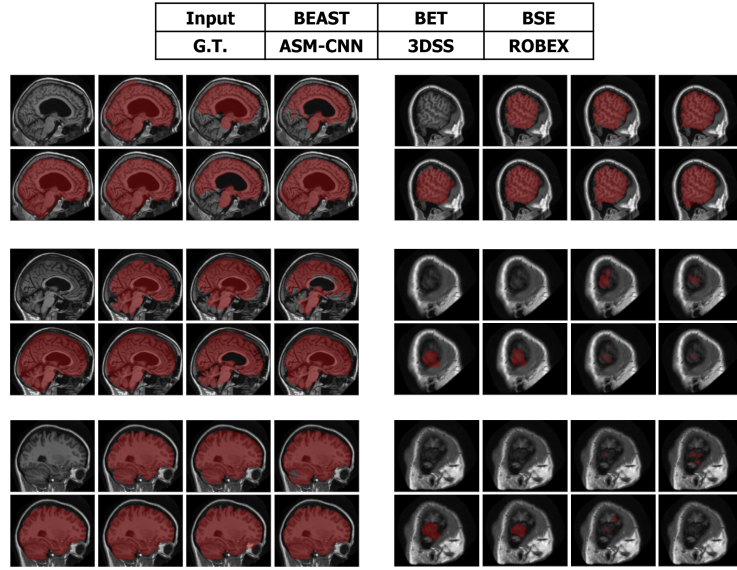


Figure 12: The comparison between ASMCNN with other methods on OASIS dataset.

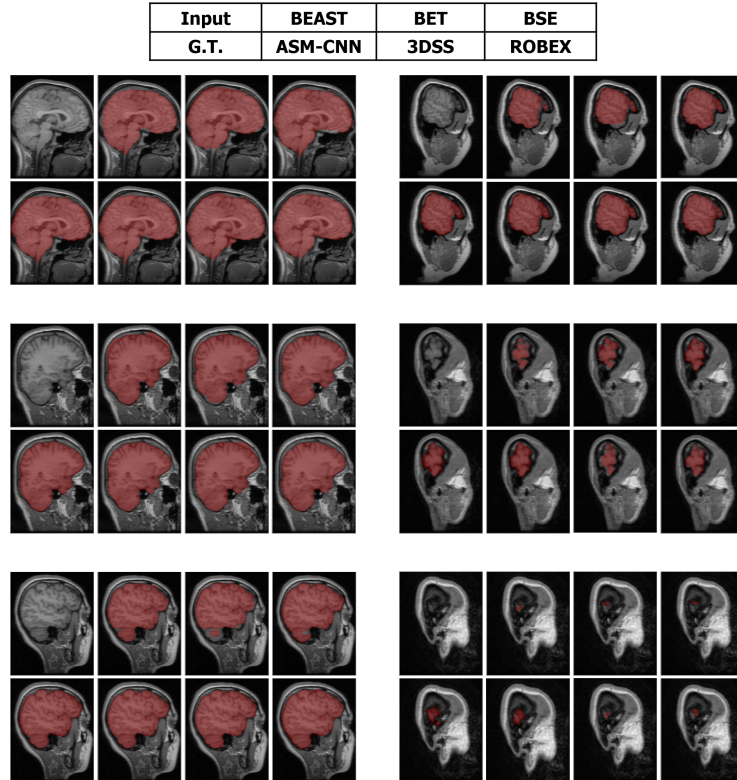


Figure 13: The comparison between ASMCNN with other methods on LPBA dataset.

brains (Figure 11). The method does not avoid a few false negatives and false
 360 positives in this group on account of the complexity of the brain structure. Nevertheless, ASMCNN can mostly obtain a better performance than others with higher accuracy.

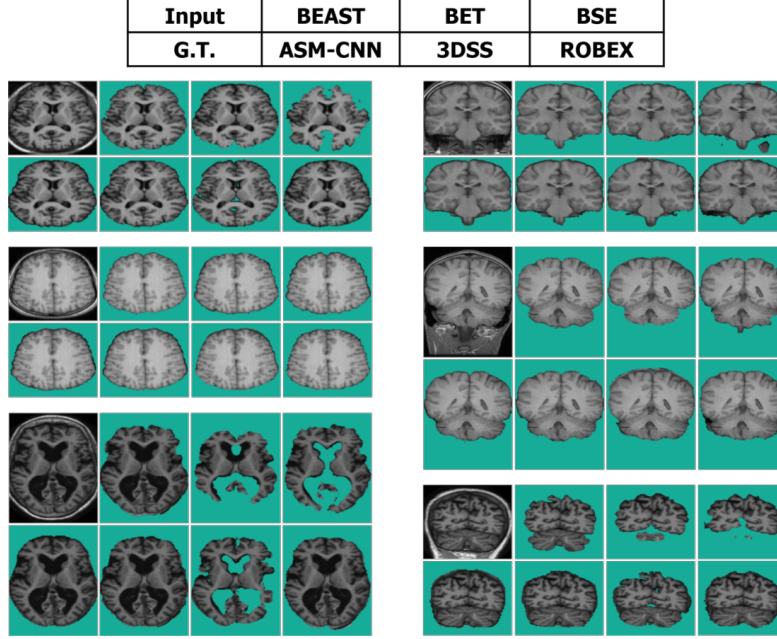


Figure 14: Resulting images on transverse and coronal plane for IBSR, LPBA, OASIS dataset.

3.4. Quantitative evaluation

Tables 2, 3, and 4 display the average value and the standard deviation of
 365 all the evaluation metrics for IBSR, LPBA, and OASIS datasets on 2D plane respectively. Similarly, Tables 5, 6, and 7 show the accuracy of segmented results on 3D structures. All results by different metrics with the list of evaluation methods on three datasets are depicted by box plots in Figures 15-20.

As the proposed approach works with 2D scans, we formulate the segmented
 370 results on 3D structures by other algorithms as sequences of 2D images in the sagittal plane for an appropriate evaluation. BEAST has the highest mean of Specificity with a small standard deviation for three datasets, although there is

Table 2: 2D Results of different methods in IBSR dataset.

Method	Dice	Jaccard	Average Hausdorff	Sensitivity	Specificity
BET	87.99 ± 0.105	79.68 ± 0.123	1.16 ± 0.55	80.76 ± 0.123	99.53 ± 0.004
BSE	85.23 ± 0.166	77.17 ± 0.206	0.85 ± 0.41	78.90 ± 0.216	99.36 ± 0.008
3DSS	91.42 ± 0.133	85.99 ± 0.149	0.72 ± 0.22	88.21 ± 0.156	99.1 ± 0.01
ROBEX	94.32 ± 0.081	90.02 ± 0.104	0.61 ± 0.24	95.22 ± 0.094	98.38 ± 0.016
BEAST	90.00 ± 0.165	84.46 ± 0.18	0.61 ± 0.15	84.63 ± 0.18	99.93 ± 0.001
ASMCNN	94.89 ± 0.063	90.82 ± 0.092	0.57 ± 0.15	93.24 ± 0.085	99.36 ± 0.007

Table 3: 2D Results of different methods in LPBA dataset.

Method	Dice	Jaccard	Average Hausdorff	Sensitivity	Specificity
BET	93.25 ± 0.084	88.17 ± 0.108	0.72 ± 0.28	89.69 ± 0.107	99.34 ± 0.006
BSE	94.37 ± 0.103	90.63 ± 0.135	0.57 ± 0.32	92.41 ± 0.136	99.33 ± 0.007
3DSS	92.47 ± 0.139	87.93 ± 0.153	0.75 ± 0.21	91.46 ± 0.161	98.22 ± 0.016
ROBEX	93.85 ± 0.127	90.12 ± 0.145	0.62 ± 0.17	92.53 ± 0.148	99.08 ± 0.006
BEAST	93.00 ± 0.135	88.83 ± 0.154	0.62 ± 0.16	89.65 ± 0.154	99.67 ± 0.006
ASMCNN	95.39 ± 0.07	91.87 ± 0.103	0.57 ± 0.19	94.72 ± 0.07	99.33 ± 0.01

Table 4: 2D Results of different methods in OASIS dataset.

Method	Dice	Jaccard	Average Hausdorff	Sensitivity	Specificity
BET	85.34 ± 0.132	76.17 ± 0.154	1.91 ± 0.77	78.17 ± 0.158	98.9 ± 0.011
BSE	85.53 ± 0.117	76.18 ± 0.145	1.94 ± 0.7	78.45 ± 0.15	98.80 ± 0.013
3DSS	87.30 ± 0.145	79.64 ± 0.173	1.81 ± 0.67	82.91 ± 0.178	98.48 ± 0.014
ROBEX	93.44 ± 0.088	88.59 ± 0.112	1.27 ± 0.27	92.1 ± 0.104	98.44 ± 0.105
BEAST	88.56 ± 0.142	81.49 ± 0.163	1.59 ± 0.37	82.71 ± 0.164	99.26 ± 0.001
ASMCNN	95.07 ± 0.054	91.04 ± 0.085	1.13 ± 0.42	94.36 ± 0.071	98.53 ± 0.015

Table 5: 3D Results of different methods in IBSR dataset.

Method	Dice	Jaccard	Average Hausdorff	Sensitivity	Specificity
BET	89.63 ± 0.035	81.39 ± 0.059	34.99 ± 6.57	82.53 ± 0.057	99.57 ± 0.002
BSE	88.48 ± 0.09	80.50 ± 0.144	32.06 ± 11.76	82.09 ± 0.157	99.42 ± 0.005
3DSS	94.56 ± 0.019	89.75 ± 0.035	24.05 ± 2.01	92.02 ± 0.048	99.18 ± 0.006
ROBEX	96.24 ± 0.012	92.78 ± 0.021	22.72 ± 3.24	97.14 ± 0.015	98.47 ± 0.012
BEAST	94.46 ± 0.021	89.57 ± 0.037	22.27 ± 2.81	89.76 ± 0.038	99.93 ± 0.0004
ASMCNN	96.51 ± 0.009	93.27 ± 0.018	20.63 ± 1.05	95.04 ± 0.027	99.39 ± 0.004

Table 6: 3D Results of different methods in LPBA dataset.

Method	Dice	Jaccard	Average Hausdorff	Sensitivity	Specificity
BET	95.19 ± 0.017	90.87 ± 0.031	26.52 ± 4.88	92.33 ± 0.032	99.40 ± 0.002
BSE	96.19 ± 0.053	93.09 ± 0.086	21.17 ± 8.38	94.66 ± 0.091	99.39 ± 0.003
3DSS	95.85 ± 0.005	92.04 ± 0.009	24.52 ± 2.34	95.90 ± 0.007	98.41 ± 0.006
ROBEX	96.91 ± 0.002	94.00 ± 0.003	21.88 ± 1.02	96.18 ± 0.008	99.13 ± 0.003
BEAST	96.47 ± 0.006	93.20 ± 0.011	21.11 ± 1.99	93.93 ± 0.01	99.72 ± 0.004
ASMCNN	97.14 ± 0.007	94.46 ± 0.013	20.15 ± 2.10	96.14 ± 0.016	99.33 ± 0.003

Table 7: 3D Results of different methods in OASIS dataset.

Method	Dice	Jaccard	Average Hausdorff	Sensitivity	Specificity
BET	87.99 ± 0.064	79.09 ± 0.095	46.42 ± 9.81	80.73 ± 0.103	98.98 ± 0.008
BSE	88.27 ± 0.048	79.32 ± 0.075	46.16 ± 7.44	81.15 ± 0.087	98.87 ± 0.011
3DSS	90.26 ± 0.07	82.93 ± 0.107	40.54 ± 10.32	85.39 ± 0.121	98.57 ± 0.01
ROBEX	95.64 ± 0.008	91.66 ± 0.015	30.31 ± 1.93	94.36 ± 0.025	98.49 ± 0.008
BEAST	92.72 ± 0.014	86.45 ± 0.025	35.65 ± 2.65	87.59 ± 0.03	99.33 ± 0.008
ASMCNN	96.50 ± 0.009	93.25 ± 0.016	26.17 ± 2.23	95.82 ± 0.019	98.58 ± 0.006

no significant difference between six methods at this evaluation metric. From the result tables, we see that ASMCNN achieves the best performance with the highest average of Dice overlap (with 0.57 - 1.63% more upper than the second one), Jaccard index (0.8 - 2.45 % higher), and AHD on three datasets. The proposed approach gets the best Sensitivity on both LPBA and OASIS datasets, while ROBEX produces the highest on the IBSR dataset. Besides, BSE also achieves the same AHD score on the LPBA dataset similar to ASMCNN, but its standard deviation is higher than us (0.32 in comparison with 0.19). It turns out that ASMCNN has an outstanding performance in all evaluation metrics and gets the smallest standard deviation in the Dice coefficient, Jaccard index, and Sensitivity. Consequently, the experimental results illustrate the consistency of our method.

Although processing with a 2D plane, we can construct 3D results by combining sequences of scans to make ASMCNN more comparable with other algo-

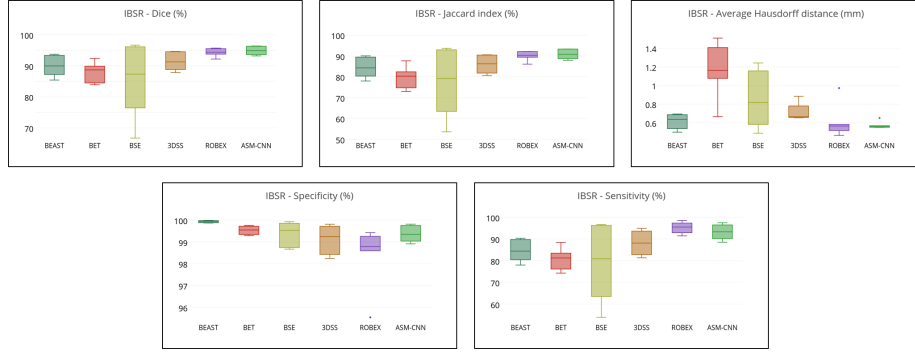


Figure 15: The 2D Box plots of Dice coefficient, Jaccard index, Average Hausdorff distance, Sensitivity and Specificity for IBSR dataset.

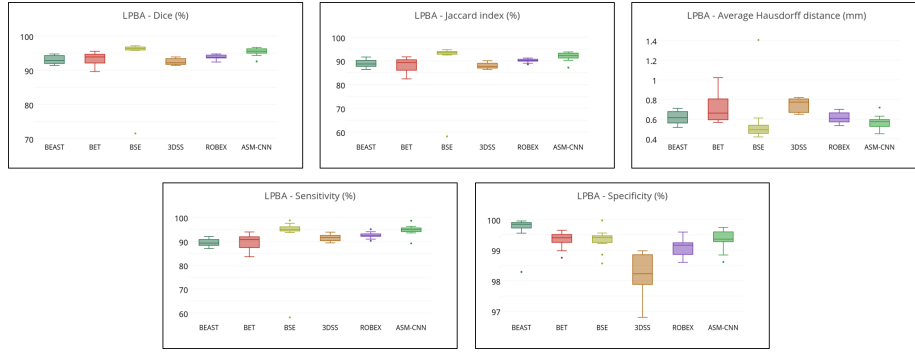


Figure 16: The 2D Box plots of Dice coefficient, Jaccard index, Average Hausdorff distance, Sensitivity and Specificity for LPBA dataset.

rithms. There is an increase in the accuracy of five remaining methods in this type of evaluation with significant improvement at standard deviation. Among other algorithms, BEAST has major changes in its accuracy for several evaluated metrics on three datasets. For instance, it approximately gains more 3.47 - 5.1% on Dice coefficients, Jaccard indexes, and Sensitivity values. Furthermore, BEAST still provides the highest Specificity, which is almost 100% for all datasets. Meanwhile, ROBEX continually obtains the best scores in Sensitivity on two datasets IBSE and LPBA. It is worth emphasizing that the 3D results produced by ASMCNN are remarkable and competitive with others. It preserves an impressive performance that gets the best scores on three datasets at the Dice coefficient, Jaccard index, AHD, and OASIS at Sensitivity.

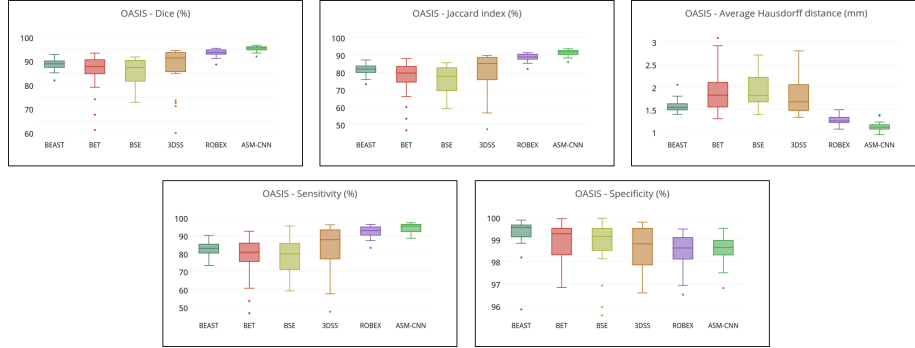


Figure 17: The 2D Box plots of Dice coefficient, Jaccard index, Average Hausdorff distance, Sensitivity and Specificity for OASIS dataset.

The box-plots in Figure 15 and 18 visualize that BSE has a big interquartile range on IBSR which means the results given from it are more disperse and have a larger variance than other techniques. However, this method has the best performance on LPBA (Figure 16, Figure 19) which gives extremely accurate results and better than others although it has a terrible outlier (about 72% at Dice overlap for 2D evaluation). Indeed, this issue is mentioned above that BSE can provide very accurate segmentations and may give atrocious results based on tuning employed parameters. By contrast, ASMCNN shows it can be durable and unaffected by datasets that outperform than others with high accuracy and small interquartile range as well as the standard deviation on three datasets, especially on OASIS (Figure 17, Figure 20). Unfortunately, its Specificity is worse than several methods. However, it can be improved by employing a suitable post-processing method to mitigate several false positives in the segmentations.

Table 8: 3D combined results of different methods for IBSR, LPBA, and OASIS dataset.

Method	Dice	Sensitivity	Specificity
2D-Unet (Dong et al. [20])	94.36 ± 0.03	95.45 ± 0.01	96.87 ± 0.01
3D-CNN (Kleesiek et al. ([19])	95.19 ± 0.01	96.25 ± 0.02	99.24 ± 0.003
ASMCNN	97.03 ± 0.01	95.80 ± 0.02	99.38 ± 0.01

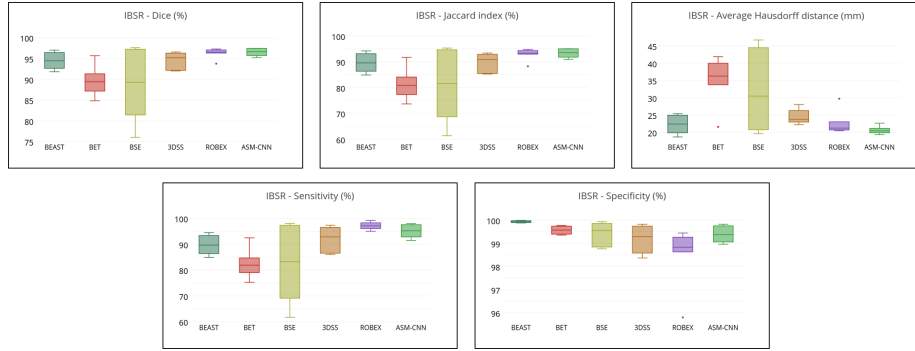


Figure 18: The 3D Box plots of Dice coefficient, Jaccard index, Average Hausdorff distance, Sensitivity and Specificity for IBSR dataset.

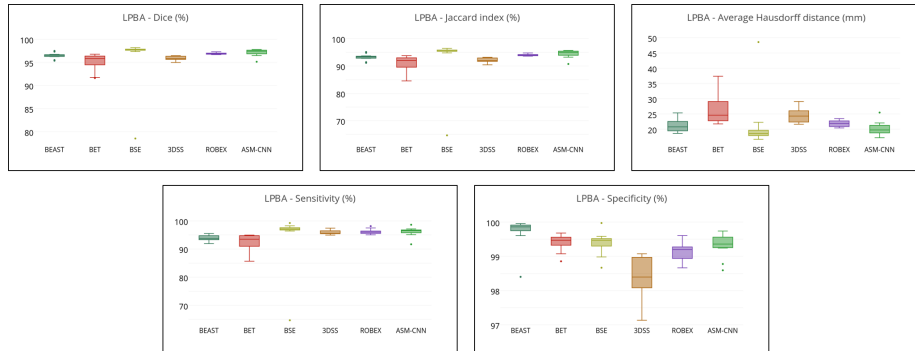


Figure 19: The 3D Box plots of Dice coefficient, Jaccard index, Average Hausdorff distance, Sensitivity and Specificity for LPBA dataset.

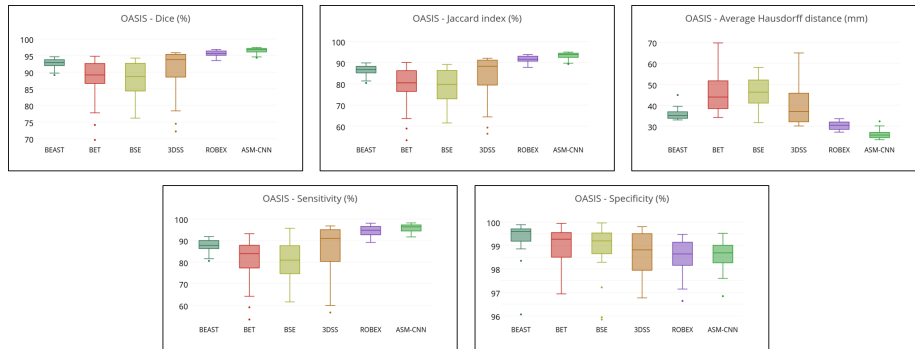


Figure 20: The 3D Box plots of Dice coefficient, Jaccard index, Average Hausdorff distance, Sensitivity and Specificity for OASIS dataset.

Comparing with other deep learning methods

As results 3D-CNN in [19] only have Dice, Sensitivity, and Specificity scores for IBSR, LPBA, and OASIS datasets, we measured results of the 2D-Unet [20] method on these three metrics. The results are shown in Table 8.

The experimental results indicate that our method achieved the highest scores on both Dice and Specificity with 97.03% and 99.38%, respectively, while 3D-CNN gained the best value in Sensitivity at 96.25%.

3.5. Ablation Study

In this section, we analyze the contribution of the following factors: (i) the effectiveness of the combination of ASM with CNN to achieve prediction results, (ii) the advantages of the grouping mechanism to operate on three different groups rather than a single one and finally (iii) the contribution of CRF post-processing step. For (i), we experimented with two distinct cases: (i.a) training a single CNN-based model (Figure 6) to predict for each pixel in all three groups and following by described post-processing steps; (i.b) utilized only ASM results without further refining by CNN to produce Group II and Group III predictions while remaining other components. For (ii), due to the large deformation of the Group I compared to other ones (Figures 2 and 3), the ASM could not learn a single principal shape simultaneously for all regions. We thus experimented by learning an ASM model for only Group II and Group III. All other steps, such as correcting with CNN or post-processing steps, were retained to highlight the grouping’s role. Lastly, factor (iii) was checked by eliminating the CRF-step for both three regions to obtain final binary masks.

We reported the average 3D results across all datasets for those settings in Table 9. One could observe that without grouping images, our performance declined dramatically from 97.03% and 95.80% down to 92.93% and 88.12% for Dice and Sensitivity, respectively. A similar trend also occurred without applying CNN or ASM, although it was lighter. Precisely, the Dice and Sensitivity metric decreased by 1.60%/2.0% and 3.07%/2.04% without CNN/ASM

respectively. On the Specificity metric, our full settings also hold the best values than other options with the deviation from small (0.25%, w/out CNN) to a large margin (3.49%, w/out ASM). This phenomenon showed that the CNN-based approach solely tends to recognize the location of skull tissues as brain tissues, resulting from the lack of global shape features from the ASM model. Lastly, the CRF component contributed significantly to the final performance, thereby improving Dice and Sensitivity from 95.69%/94.63% to 97.03%/95.80% correspondingly. Though there was a small reduction in the Specificity metric; however, the deviation was not significant.

Table 9: 3D combined results of the ablation study for IBSR, LPBA, and OASIS dataset.

Method	Dice	Sensitivity	Specificity
ASMCNN (Without ASM)	94.13 ± 0.01	93.76 ± 0.01	95.89 ± 0.02
ASMCNN (Without CNN)	95.43 ± 0.01	92.73 ± 0.02	99.13 ± 0.01
ASMCNN (Without Grouping)	92.93 ± 0.03	88.12 ± 0.06	98.26 ± 0.01
ASMCNN (Without CRF)	95.69 ± 0.01	94.63 ± 0.02	99.41 ± 0.01
ASMCNN (Full Settings)	97.03 ± 0.01	95.80 ± 0.02	99.38 ± 0.01

In short, all empirical pieces of evidence can be argued by the properties of employed algorithms. Firstly, without grouping shapes, our curve evolution based on ASM easily was stuck in a local optimum, leading to a massive discrepancy between the prediction and ground-truth targets, which is too difficult to improve by CNN. This phenomenon was also similar to the results of the BET algorithm depicted in Figures 11 and 12 (the top left pictures), in which the curve was stopped at the inner boundary inside the brain because of a confusion between this temporary state with a target shape learned from the training set. One of the causes for this confusion is that we trained a statistical shape model using patterns that differ significantly in shape and appearance, resulting in learned models that could not accurately capture the variation between regions. Secondly, utilizing ASM solely on separated regions may create over-smooth results; thereby, fine-grant details along the image boundary usually were skipped. In such situations, refining steps are necessary to compensate for this shortfall

(Figure 10). In the opposite direction, the CNN-based strategy for each pixel using only local features could not consider important factors such as the consistency of brain shape and global appearances, implying incorrect predictions of skull-tissues with brain-tissues. Finally, the CRF post-processing steps allow further refining segmented results in terms of global consistency in appearance aspects, complementing for potential errors of CNN’s local-based approaches.

4. Discussion

Our Strengths and Limitations. We applied the divide-and-conquer strategy, which was inspired by exploiting brain regions’ symmetric regions in the sagittal plane (Figure 3). By this, images belong to a particular group share similar attributes such as shapes and deformation along its boundaries, which was then leveraged to compose proper solutions to optimize final results. It involves (i) capturing global shapes (by ASM) and refining details with local features (by CNN) for Groups II, III and (ii) learning a curve (by Gaussian Process) to adjust brain center points through connecting prior medical knowledge and current masks obtained from (i). In short, these mechanisms permit us a flexible way to control segmentation quality effectively in each group by taking into account desired characteristics during training and prediction procedure. Such properties are essential as dealing with small brain regions whose shapes are complex as Group I. However, the proposed method also has some significant limitations. Firstly, ASMCNN requires more annotation efforts to train the whole system. In specific, besides labeled masks for each image (or labeled 3D volume) as default in segmentation task, we need further two kinds of data, including four image indexes (Algorithm 1) denoting for borderlines among groups and four ratio values for extracting bounding boxes which comprise specific features to highlight variations between disparate regions (Figure 4). Secondly, our method also demands user to input some hyper-parameters, for instance in *CheckCenter* function (Algorithm 6), *CheckDistance* function (Algorithm 8) and in conditional random field post-processing. However, this requirement can

also be considered an ASMCNN’s feature since users can adjust the parameters to obtain the best results under different image acquisition conditions. Finally,
 495 for regions II and III, the CNN steps have to wait until the ASM procedure ending, or in Group I, we can only produce final predictions given obtained masks from Groups II and III. This sequential fashion results in our method being slower than the end-to-end deep network-based approach.

Comparing with Other Baselines. In the non-deep network category, ROBEX is
 500 the second-best method, following our ASMCNN in most metrics. This method runs directly on the 3D volume by evolving a point distribution model-based curve and could capture brain regions’ s 3D global structure stably. However, in practice, the target brain shape is not perfectly represented; ROBEX thus usually ignores or over-segments small and complicated regions (Figure 12 and 13,
 505 bottom right images). Simultaneously, with ASMCNN, we can overcome such challenges by adapting specific rules for Group I. To fix these harmful errors, ROBEX needs to improve further output contours driven by deep features as our approach with CNN. Unfortunately, training such networks is challenging due to the insufficient data if we work directly in 3D space instead of 2D slices. For
 510 instance, in our experiments, we have 103 3D volume samples for all datasets, compared to approximately 17000 2D images extracting from 3D volumes. Such a massive difference in the amount of data explains why a 2D based approach like ASMCNN could offer a greater benefit to training a dedicated deep network for correcting object boundaries. In the deep network category, 2D-Unet
 515 and 3D-CNN provide a convenient and efficient way to generate segmentation results by learning only labeled ground-truths. However, both methods predict binary masks by considering only local features; hence it is quite sensitive to noise regions whose gray levels closely resemble brain regions due to the image acquisition’s errors. In contrast, our ASMCNN considers both global structure
 520 information by ASM and local features by utilizing the power of deep features in CNN, which implies a more robust and reliable pipeline.

Future Work. In our flowchart, ASM plays a role in preserving the principal shapes. However, ASM could only work effectively when the objects' shapes are similar to the trained active appearance model. Therefore, the algorithm may
525 likely produce poorer results when processing unusual shapes. Unfortunately, in medical imaging, the data are usually obscured by noise due to limitations of image acquisition systems, or the shapes and the distribution of images are not included in training data. In such cases, ASM may produce severely imprecise boundaries; even CNN cannot verify or refine. We intend to investigate
530 techniques based on deep learning to construct better models for shape and appearance in future work. In another direction, working on the whole 3D brain volume is also a promising approach. To this end, we can extend 3D-ASM [44] based methods so that prior medical knowledge, for example, symmetry property across two hemispheres, is considered during the curve evolution. Besides,
535 learning optimal features along the object's profiles could be enhanced by leveraging deep features. Finally, modifying CNN-based refining strategies to make it more robust in 3D volume could be achieved by generalizing our architecture in Figure 6 from pixels to voxel input and combining transfer learning techniques.

5. Conclusion

540 This article has proposed a novel approach for brain extraction in magnetic resonance images, namely ASMCNN, by associating two main components: Active Shape Model and Convolutional Neural Network. Unlike existing methods, ASMCNN processes 2D sequences of images instead of using 3D brain structures. For each 2D scan, a rough estimation of the brain region is estimated by
545 ASM. Its boundary is then refined by a CNN, which is constructed and trained with special rules. Finally, the brain region is post-processed by CRFs, Gaussian processes, and special rules. Our proposed approach has shown its consistency in performance; mainly, it can produce highly accurate segmentations in all cases, even when brain regions are small and scattered. In the experiments, our
550 method has achieved remarkable for the whole three datasets (IBSR, LPBA,

and OASIS) in 2D scans and 3D structures and surpassed the performance of seven other state-of-the-art methods.

References

- [1] S. Jiang, W. Zhang, Y. Wang, Z. Chen, Brain extraction from cerebral
555 MRI volume using a hybrid level set based active contour neighborhood
model, *BioMedical Engineering OnLine* 12 (1) (2013) 31. doi:10.1186/
1475-925X-12-31.
- [2] J. A. Maldjian, J. B. Daunais, D. P. Friedman, C. T. Whitlow, Vervet MRI
atlas and label map for fully automated morphometric analyses, *Neuroin-*
560 *formatics* 12 (4) (2014) 543–550. doi:10.1007/s12021-014-9231-8.
- [3] A. M. Dale, B. Fischl, M. I. Sereno, Cortical surface-based analysis: I.
segmentation and surface reconstruction, *NeuroImage* 9 (2) (1999) 179–
194. doi:10.1006/nimg.1998.0395.
- [4] S. Sharma, V. Noblet, F. Rousseau, F. Heitz, L. Rumbach, J.-P. Armspach,
565 Evaluation of brain atrophy estimation algorithms using simulated ground-
truth data, *Medical Image Analysis* 14 (3) (2010) 373–389. doi:10.1016/
j.media.2010.02.002.
- [5] P. Kalavathi, V. B. S. Prasath, Methods on skull stripping of MRI head
scan images—a review, *Journal of Digital Imaging* 29 (3) (2016) 365–379.
570 doi:10.1007/s10278-015-9847-8.
- [6] S. Roy, J. A. Butman, D. L. Pham, Robust skull stripping using multiple
MR image contrasts insensitive to pathology, *NeuroImage* 146 (2017) 132–
147. doi:10.1016/j.neuroimage.2016.11.017.
- [7] R. Beare, J. Chen, C. Adamson, T. Silk, D. Thompson, J. Yang, V. An-
575 derson, M. Seal, A. Wood, Brain extraction using the watershed trans-
form from markers, *Frontiers in Neuroinformatics* 7 (2013) 32. doi:
10.3389/fninf.2013.00032.

- [8] J. Hwang, Y. Han, H. Park, Skull-stripping method for brain MRI using a 3D level set with a speedup operator, *Journal of Magnetic Resonance Imaging* 34 (2) (2011) 445–456. doi:10.1002/jmri.22661.
- [9] A. G. Balan, A. J. Traina, M. X. Ribeiro, P. M. Marques, C. T. Jr., Smart histogram analysis applied to the skull-stripping problem in t1-weighted MRI, *Computers in Biology and Medicine* 42 (5) (2012) 509–522. doi:10.1016/j.combiomed.2012.01.004.
- [10] N. Sharma, L. M. Aggarwal, Automated medical image segmentation techniques, *Journal of medical physics/Association of Medical Physicists of India* 35 (1) (2010) 3.
- [11] J. E. Iglesias, C. Y. Liu, P. M. Thompson, Z. Tu, Robust brain extraction across datasets and comparison with publicly available methods, *IEEE Transactions on Medical Imaging* 30 (9) (2011) 1617–1634. doi:10.1109/TMI.2011.2138152.
- [12] Y. Wang, J. Nie, P.-T. Yap, F. Shi, L. Guo, D. Shen, Robust deformable-surface-based skull-stripping for large-scale studies, in: *Proceedings of the 14th International Conference on Medical Image Computing and Computer-assisted Intervention - Volume Part III*, Springer-Verlag, Berlin, Heidelberg, 2011, pp. 635–642.
- [13] K. K. Leung, J. Barnes, M. Modat, G. R. Ridgway, J. W. Bartlett, N. C. Fox, S. Ourselin, Brain MAPS: an automated, accurate and robust brain extraction technique using a template library, *NeuroImage* 55 (3) (2011) 1091–1108. doi:10.1016/j.neuroimage.2010.12.067.
- [14] B. B. Avants, N. J. Tustison, M. Stauffer, G. Song, B. Wu, J. C. Gee, The insight toolkit image registration framework, *Frontiers in Neuroinformatics* 8 (2014) 44. doi:10.3389/fninf.2014.00044.
- [15] R. A. Heckemann, C. Ledig, K. R. Gray, P. Aljabar, D. Rueckert, J. V. Hajnal, A. Hammers, Brain extraction using label propagation and group

agreement: Pincram, PLOS ONE 10 (7) (2015) 1–18. doi:10.1371/
journal.pone.0129211.

- [16] S. K. Warfield, K. H. Zou, W. M. Wells, Simultaneous truth and performance level estimation (STAPLE): an algorithm for the validation of image segmentation, IEEE Transactions on Medical Imaging 23 (7) (2004) 903–921. doi:10.1109/TMI.2004.828354.
- [17] S. F. Eskildsen, P. Coupé, V. Fonov, J. V. Manjón, K. K. Leung, N. Guizard, S. N. Wassef, L. R. Østergaard, D. L. Collins, BEaST: brain extraction based on nonlocal segmentation technique, NeuroImage 59 (3) (2012) 2362–2373. doi:10.1016/j.neuroimage.2011.09.012.
- [18] O. Ronneberger, P. Fischer, T. Brox, U-net: Convolutional networks for biomedical image segmentation, in: International Conference on Medical image computing and computer-assisted intervention, Springer, 2015, pp. 234–241.
- [19] J. Kleesiek, G. Urban, A. Hubert, D. Schwarz, K. Maier-Hein, M. Bendszus, A. Biller, Deep mri brain extraction: a 3d convolutional neural network for skull stripping, NeuroImage 129 (2016) 460–469.
- [20] H. Dong, G. Yang, F. Liu, Y. Mo, Y. Guo, Automatic brain tumor detection and segmentation using u-net based fully convolutional networks, in: annual conference on medical image understanding and analysis, Springer, 2017, pp. 506–517.
- [21] B. Menze, A. Jakab, S. Bauer, J. Kalpathy-Cramer, K. Farahani, J. Kirby, Y. Burren, N. Porz, J. Slotboom, R. Wiest, L. Lanczi, E. Gerstner, M.-A. Weber, T. Arbel, B. Avants, N. Ayache, P. Buendia, L. Collins, N. Cordier, J. Corso, A. Criminisi, T. Das, H. Delingette, C. Demiralp, C. Durst, M. Dojat, S. Doyle, J. Festa, F. Forbes, E. Geremia, B. Glocker, P. Golland, X. Guo, A. Hamamci, K. Iftekharuddin, R. Jena, N. John, E. Konukoglu, D. Lashkari, J. Antonio Mariz, R. Meier, S. Pereira, D. Precup, S. J. Price, T. Riklin-Raviv, S. Reza, M. Ryan, L. Schwartz, H.-C.

- 635 Shin, J. Shotton, C. Silva, N. Sousa, N. Subbanna, G. Szekely, T. Taylor,
O. Thomas, N. Tustison, G. Unal, F. Vasseur, M. Wintermark, D. Hye Ye,
L. Zhao, B. Zhao, D. Zikic, M. Prastawa, M. Reyes, K. Van Leemput,
The Multimodal Brain Tumor Image Segmentation Benchmark (BRATS),
IEEE Transactions on Medical Imaging (2014) 33doi:10.1109/TMI.2014.
640 2377694.
URL <https://hal.inria.fr/hal-00935640>
- [22] A. Ortiz, J. Gorriz, J. Ramirez, D. Salas-Gonzalez, Improving mr
brain image segmentation using self-organising maps and entropy-
gradient clustering, Information Sciences 262 (2014) 117 – 136.
645 doi:<https://doi.org/10.1016/j.ins.2013.10.002>.
URL [http://www.sciencedirect.com/science/article/pii/
S0020025513007111](http://www.sciencedirect.com/science/article/pii/S0020025513007111)
- [23] F. Binczyk, B. Stjelties, C. Weber, M. Goetz, K. Meier-Hein, H.-P.
Meinzer, B. Bobek-Billewicz, R. Tarnawski, J. Polanska, Mimseg - an
650 algorithm for automated detection of tumor tissue on nmr apparent
diffusion coefficient maps., Information Sciences 384 (2017) 235 – 248.
doi:<https://doi.org/10.1016/j.ins.2016.07.052>.
URL [http://www.sciencedirect.com/science/article/pii/
S0020025516305345](http://www.sciencedirect.com/science/article/pii/S0020025516305345)
- 655 [24] T. Cootes, C. Taylor, D. Cooper, J. Graham, Active shape models-their
training and application, Computer Vision and Image Understanding 61 (1)
(1995) 38–59. doi:10.1006/cviu.1995.1004.
- [25] Y. Lecun, L. Bottou, Y. Bengio, P. Haffner, Gradient-based learning ap-
plied to document recognition, Proceedings of the IEEE 86 (11) (1998)
660 2278–2324. doi:10.1109/5.726791.
- [26] F. H. Netter, Atlas of human anatomy, Professional Edition E-Book: in-
cluding NetterReference. com Access with full downloadable image Bank,
Elsevier Health Sciences, 2014.

- [27] N. Dalal, B. Triggs, Histograms of oriented gradients for human detection,
 665 in: 2005 IEEE Computer Society Conference on Computer Vision and Pat-
 tern Recognition (CVPR'05), IEEE Computer Society, Washington, DC,
 USA, 2005, pp. 886–893 vol. 1.
- [28] D.-R. Chen, Q. Wu, Y. Ying, D.-X. Zhou, Support vector machine soft
 margin classifiers: error analysis, *Journal of Machine Learning Research*
 670 5 (Sep) (2004) 1143–1175.
- [29] N. S. Altman, An introduction to kernel and nearest-neighbor nonpara-
 metric regression, *The American Statistician* 46 (3) (1992) 175–185. doi:
 10.1080/00031305.1992.10475879.
- [30] B. Van Ginneken, A. F. Frangi, J. J. Staal, B. M. ter Haar Romeny, M. A.
 675 Viergever, Active shape model segmentation with optimal features, *IEEE*
transactions on medical imaging 21 (8) (2002) 924–933. doi:10.1109/TMI.
 2002.803121.
- [31] H. B. Mann, D. R. Whitney, On a test of whether one of two random vari-
 ables is stochastically larger than the other, *The Annals of Mathematical*
 680 *Statistics* 18 (1) (1947) 50–60. doi:10.1214/aoms/1177730491.
- [32] X. Liu, F. Chen, Automatic segmentation of 3-d brain mr images by using
 global tissue spatial structure information, *IEEE Transactions on Applied*
Superconductivity 24 (5) (2014) 1–5. doi:10.1109/TASC.2014.2347316.
- [33] K. He, X. Zhang, S. Ren, J. Sun, Delving deep into rectifiers: Surpassing
 685 human-level performance on imagenet classification, in: *Proceedings of the*
IEEE international conference on computer vision, 2015, pp. 1026–1034.
- [34] C. Rasmussen, *Cki williams gaussian processes for machine learning mit*
 press, Cambridge, MA.
- [35] Ibsr dataset <http://www.nitrc.org/projects/ibsr>.

- [36] P. Krähenbühl, V. Koltun, Efficient inference in fully connected CRFs with gaussian edge potentials, in: Proceedings of the 24th International Conference on Neural Information Processing Systems, Curran Associates Inc., USA, 2011, pp. 109–117.
- [37] S. M. Smith, Fast robust automated brain extraction, Human Brain Mapping 17 (3) (2002) 143–155. doi:10.1002/hbm.10062.
- [38] D. W. Shattuck, S. R. Sandor-Leahy, K. A. Schaper, D. A. Rottenberg, R. M. Leahy, Magnetic resonance image tissue classification using a partial volume model, NeuroImage 13 (5) (2001) 856–876. doi:10.1006/nimg.2000.0730.
- [39] R. W. Cox, AFNI: software for analysis and visualization of functional magnetic resonance neuroimages, Computers and Biomedical Research 29 (3) (1996) 162–173. doi:10.1006/cbmr.1996.0014.
- [40] Lpba dataset <http://sve.loni.ucla.edu/>.
- [41] Oasis dataset <http://www.oasis-brains.org/>.
- [42] M. Abadi, A. Agarwal, P. Barham, E. Brevdo, Z. Chen, C. Citro, G. S. Corrado, A. Davis, J. Dean, M. Devin, S. Ghemawat, I. Goodfellow, A. Harp, G. Irving, M. Isard, Y. Jia, R. Jozefowicz, L. Kaiser, M. Kudlur, J. Levenberg, D. Mané, R. Monga, S. Moore, D. Murray, C. Olah, M. Schuster, J. Shlens, B. Steiner, I. Sutskever, K. Talwar, P. Tucker, V. Vanhoucke, V. Vasudevan, F. Viégas, O. Vinyals, P. Warden, M. Wattenberg, M. Wicke, Y. Yu, X. Zheng, TensorFlow: Large-scale machine learning on heterogeneous systems, software available from tensorflow.org (2015). URL <http://tensorflow.org/>
- [43] J. Bertels, T. Eelbode, M. Berman, D. Vandermeulen, F. Maes, R. Bisschops, M. B. Blaschko, Optimizing the dice score and jaccard index for medical image segmentation: Theory and practice, in: International Con-

ference on Medical Image Computing and Computer-Assisted Intervention, Springer, 2019, pp. 92–100.

[44] T. Heimann, I. Wolf, T. Williams, H.-P. Meinzer, 3d active shape models using gradient descent optimization of description length, in: Biennial International Conference on Information Processing in Medical Imaging, Springer, 2005, pp. 566–577.

[45] N. Dalal, B. Triggs, Histograms of oriented gradients for human detection, in: 2005 IEEE computer society conference on computer vision and pattern recognition (CVPR'05), Vol. 1, IEEE, 2005, pp. 886–893.

Appendices

Table 10: List of notations used in Algorithms 1 and 2.

Notation	Remark
$P = \{p_1, p_2, \dots, p_m\}$	The set of people in each dataset where p_i ($1 \leq i \leq m$) is the i^{th} person.
$N = \{n_1, n_2, \dots, n_m\}$	n_j is the number of 2D images for each person p_j ($1 \leq j \leq m$).
$I_{p_j} = \{I_{p_j 1}, I_{p_j 2}, \dots, I_{p_j n_j}\}$	$I_{p_j k}$ ($1 \leq k \leq n_j$) is the k^{th} image from person p_j .
$G = \{G_I, G_{II}, G_{III}\}$	The list of groups of 2D images determined by our algorithm.
$G_{I-p_j}, G_{II-p_j}, G_{III-p_j}$	G_{k-p_j} is the list of images in group k ($k = I, II, III$) for a person p_j generated by our algorithm.
$R_i, (i \in 1, 2, 3, 4)$	The vectors indicate for the starting and ending slices for each group in training data.
$F_i, (i \in \{I, II, III\})$	The feature vectors extracted by HOG algorithm for images in group G_i
M_{12}, M_{23}	SVM models for image classification between Group I vs. II and Group II vs. III.
r_1, r_2, r_3, r_4	All rates used for estimating the starting and ending slices between different groups.

Algorithm 1: Training classifiers for clustering images into different groups

Input : P

Output: $M_{12}, M_{23}, r_1, r_2, r_3, r_4$

```

1  foreach person  $p_j \in P$  do
2      select  $k_1, k_2, k_3, k_4$  such that:
3       $A = \{I_{p_j 1}, I_{p_j 2}, \dots, I_{p_j k_1}\} \in G_{I-p_j}$ 
4       $B = \{I_{p_j k_1+1}, I_{p_j k_1+2}, \dots, I_{p_j k_2}\} \in G_{II-p_j}$ 
5       $C = \{I_{p_j k_2+1}, I_{p_j k_2+2}, \dots, I_{p_j k_3}\} \in G_{III-p_j}$ 
6       $D = \{I_{p_j k_3+1}, I_{p_j k_3+2}, \dots, I_{p_j k_4}\} \in G_{II-p_j}$ 
7       $E = \{I_{p_j k_4+1}, I_{p_j k_4+2}, \dots, I_{p_j n_j}\} \in G_{I-p_j}$ 
8      insert:
9       $G_{x-p_j}$  to vector  $G_x$  ( $x \in I, II, III$ )
10      $k_i/n_j$  to vector  $R_i$  ( $i \in 1, 2, 3, 4$ )
11 end

12 foreach group  $G_i \in G$  do
13     select constant  $r$ 
14     foreach image  $I \in G_i$  do
15          $Rec \leftarrow$  Extract rectangle containing the skull of  $I$ 
16         using mask data
17          $SubRec \leftarrow$  Extract sub rectangle from  $Rec$  with  $r$ 
18          $feature \leftarrow$  Extract features for  $I$  in  $SubRec$  with
19         HOG method [45]
20         insert  $feature$  to vector  $F_i$ 
21     end
22 end

23  $M_{12} \leftarrow$  Training a classifier model with  $F_1$ , and  $F_2$  by soft-margin SVM
24  $M_{23} \leftarrow$  Training a classifier model with  $F_2$ , and  $F_3$  by soft-margin SVM
25  $r_i \leftarrow mean(R_i); i \in 1, 2, 3, 4$ 
26 return  $M_{12}, M_{23}, r_1, r_2, r_3, r_4$ 

```

Algorithm 2: Classifying images into three groups G_I, G_{II}, G_{III}

Input : $M_{12}, M_{23}, r_1, r_2, r_3, r_4, I_{p_j}$ **Output:** $G_{I-p_j}, G_{II-p_j}, G_{III-p_j}$

```
1  $r_{i\text{new}} \leftarrow r_i \cdot n_j$  ( $i \in \{1, 2, 3, 4\}$ ),  $n_j$  is the number images of  $p_j$ 
2 for  $id \leftarrow r_{1,\text{new}} - 10$  to  $r_{1,\text{new}} + 10$  do
3   if  $M_{12}(I_{p_j id}) == 0$  then
4     insert  $A = \{I_{p_j 1}, I_{p_j 2}, \dots, I_{p_j id-1}\}$  to vector  $G_{I-p_j}$ 
5      $r_{1,\text{new}} \leftarrow id - 1$ 
6     break
7   end
8 end

9 for  $id \leftarrow r_{2,\text{new}} - 10$  to  $r_{2,\text{new}} + 10$  do
10  if  $M_{23}(I_{p_j id}) == 0$  then
11    insert  $B = \{I_{p_j r_{1,\text{new}}+1}, I_{p_j r_{1,\text{new}}+2}, \dots, I_{p_j id-1}\}$  to vector  $G_{II-p_j}$ 
12     $r_{2,\text{new}} \leftarrow id - 1$ 
13    break
14  end
15 end

16 for  $id \leftarrow r_{3,\text{new}} - 10$  to  $r_{3,\text{new}} + 10$  do
17  if  $M_{23}(I_{p_j id}) == 1$  then
18    insert  $C = \{I_{p_j r_{2,\text{new}}+1}, I_{p_j r_{2,\text{new}}+2}, \dots, I_{p_j id-1}\}$  to vector  $G_{III-p_j}$ 
19     $r_{3,\text{new}} \leftarrow id - 1$ 
20    break
21  end
22 end

23 for  $id \leftarrow r_{4,\text{new}} - 10$  to  $r_{4,\text{new}} + 10$  do
24  if  $M_{12}(I_{p_j id}) == 1$  then
25    insert  $D = \{I_{p_j r_{3,\text{new}}+1}, I_{p_j r_{3,\text{new}}+2}, \dots, I_{p_j id-1}\}$  to vector  $G_{II-p_j}$ 
26     $r_{4,\text{new}} \leftarrow id - 1$ 
27    insert  $E = \{I_{p_j r_{4,\text{new}}+1}, I_{p_j r_{4,\text{new}}+2}, \dots, I_{p_j n_j}\}$  to vector  $G_{I-p_j}$ 
28    break
29  end
30 end

31 return  $G_{I-p_j}, G_{II-p_j}, G_{III-p_j}$ 
```

Algorithm 3: *ConvertRange* – Convert a value x_{AB} in range $[A, B]$ to range $[C, D]$

Input : A, B, C, D, x_{AB}

Output: x_{CD}

1 $x_{CD} = C + (x_{AB} - A) * (D - C) / (B - A)$

2 return x_{CD}

Algorithm 4: Process Images in Group I for the p_j person

Input : $C_{p_j 1} \rightarrow C_{p_j m}, C_{p_j k+1} \rightarrow C_{p_j n_j}$: CNN resulting images of the p_j person in Group 01 from the slice $1^{th} \rightarrow m^{th}$ and $(k+1)^{th} \rightarrow n_j^{th}$.

$F_{p_j m+1}, F_{p_j k}$: two final segmentation results of the p_j person in Group II at slice $(m+1)^{th}$ and k^{th} .

GPM : Gaussian Process Model is described in subsection 2.4.

Output: Final predictions for the p_j person in Group I

$F_{p_j 1} \rightarrow F_{p_j m}, F_{p_j k+1} \rightarrow F_{p_j n_j}$

```
1  $Image_1 = F_{p_j m+1}, Image_2 = F_{p_j k}$ 
2  $\alpha = 0.4, \beta = 1.75$ 
3 for  $i \leftarrow m$  down to 1 do
4    $C_{p_j i} \leftarrow \text{Denoise in } C_{p_j i}$ 
5    $C_{p_j i} = \text{CheckCenter}(C_{p_j i}, Image_1)$ 
6    $C_{p_j i} = \text{CheckArea}(p_j i, \alpha)$ 
7    $d_i \leftarrow GPM(i_{GPM})$ 
8    $C_{p_j i} = \text{CheckDistance}(p_j i, d_i, \beta)$ 
9    $F_{p_j i} \leftarrow CRF(C_{p_j i})$ 
10   $Image_1 \leftarrow F_{p_j i}$ 
11 end
12 for  $i \leftarrow k+1$  to  $n_j$  do
13    $C_{p_j i} \leftarrow \text{Denoise in } C_{p_j i}$ 
14    $C_{p_j i} = \text{CheckCenter}(C_{p_j i}, Image_2)$ 
15    $C_{p_j i} = \text{CheckArea}(C_{p_j i}, \alpha)$ 
16    $d_i \leftarrow GPM(i_{GPM})$ 
17    $C_{p_j i} = \text{CheckDistance}(C_{p_j i}, d_i, \beta)$ 
18    $F_{p_j i} \leftarrow CRF(C_{p_j i})$ 
19    $Image_2 = F_{p_j i}$ 
20 end
21 return  $F_{p_j 1} \rightarrow F_{p_j m}, F_{p_j k+1} \rightarrow F_{p_j n_j}$ 
```

Algorithm 5: *MergeSlice*(X, Y, α)

Input : Two binary images X, Y ; Open distance α **Output:** Binary image Z created by combining X and Y

- 1 $O \leftarrow \text{OpenBoundary}(Y, \alpha)$
 - 2 $\text{Core} \leftarrow Y \setminus O$ and $\text{Boundary} \leftarrow X \cap O$
 - 3 $Z \leftarrow \text{Core} \cup \text{Boundary}$
 - 4 Apply morphology to fill small holes in Z (if exists)
 - 5 **return** Z
-

Algorithm 6: *CheckCenter* – Remove components in image X whose center is not in image Y to create image Z

Input : X, Y **Output:** Z

- 1 $Z = X$
 - 2 $\text{bbox} \leftarrow$ the smallest bounding box surrounding all components in Y
 - 3 **foreach** component c_i in Z **do**
 - 4 $\text{center}_i \leftarrow$ Coordinates of the center of c_i
 - 5 **if** center_i is not in bbox **then**
 - 6 Remove c_i out of Z
 - 7 **end**
 - 8 **end**
 - 9 **return** Z
-

Algorithm 7: *CheckArea* – Remove small components in image X with the coefficient α to create image Y

Input : X, α

Output: Y

```

1  $Y = X$ 

2 foreach component  $c_i$  in  $Y$  do
3    $a_i \leftarrow \text{Area of } c_i$ 
4 end

5  $a_{max} \leftarrow \max \{a_i\}$ 
6  $a_{threshold} = \alpha * a_{max}$ 

7 foreach component  $c_i$  in  $Y$  do
8   if  $a_i < a_{threshold}$  then
9     Remove  $c_i$  out of  $Y$ 
10  end
11 end

12 return  $Y$ 

```

Algorithm 8: *CheckDistance* – Remove components having small distance in image X with the coefficient β to create image Y

Input : X, d, β

Output: Y

```

1  $Y = X$ 

2 foreach component  $c_i$  in  $Y$  do
3    $center_i \leftarrow$  Coordinates of the center of  $c_i$ 
4    $dif_i = |d - \|center_i\|_2|$ 
5 end

6  $dif_{min} \leftarrow \min \{dif_i\}$ 
7  $dif_{threshold} = \beta * dif_{min}$ 

8 foreach component  $c_i$  in  $Y$  do
9   if  $dif_i > dif_{threshold}$  then
10    Remove  $c_i$  out of  $Y$ 
11   end
12 end

13 return  $Y$ 

```
